Rock Mechanics and Rock Engineering (2019) 52:3909–3919
https://doi.org/10.1007/s00603-019-01796-7

ORIGINAL PAPER

Stress Redistribution Monitoring Using Passive Seismic Tomography at a Deep Nickel Mine

Xu Ma[1,2] · Erik Westman[1] · Farid Malek[3] · Mike Yao[4]

Received: 4 August 2018 / Accepted: 21 March 2019 / Published online: 17 April 2019

Abstract
High magnitude seismic events (HMSE), also called major events, triggered at underground mines can severely threaten safety and structures in mines. The aims of this work are to assess stress evolution with the occurrence of them and identify patterns in stress change. Several methods were used to help understand the stress redistribution and rock mass behavior related to two HMSE with moment magnitude greater than 1.0 in a deep nickel mine. Approximately 46,500 seismic events were compiled with 2 HMSE at this mine and used seismic tomography to obtain high-resolution images and temporal-spatial velocity changes before and after these events. This work exhibited surrounding stress evolution and geological structures. Seismic imaging results show that velocity increased in the nearby regions of HMSE before they were triggered. Stress subsequently reduced in the relaxation process after the occurrence of HMSE. Conversely, regions predominantly occupied by low-velocity anomalies increased to higher stress levels after HMSE. Overall, the stress redistributed toward an equilibrium state following HMSE. This study highlights the value of utilizing seismic tomography for estimating stress evolution associated with HMSE. The findings illuminate the applications of seismic imaging around HMSE of hard-rock mines, providing insights into seismic hazard mitigation for deep mining.

Keywords Mining-induced seismicity · Seismic imaging · High magnitude seismic events (HMSE)

1 Introduction

Seismicity triggered by underground excavations at mines has been a primary concern with mining at greater depths in recent years (Malek et al. 2009; Urbancic and Trifu 2000; Vallejos and McKinnon 2011; Westman et al. 2012). Disturbed by excavations in subsurface structures, regional stress fields lose their stress balance state and the induced stress may exceed the strength of the rock mass (Brady and Brown 2013; Young et al. 2004). Seismic monitoring systems are increasingly used in the mining industry to locate and characterize seismic events (Sweby et al. 2006; Malek et al. 2008). Seismic monitoring systems can capture and determine seismicity rate, waveform arrival times, and source parameters that include magnitude, energy, and event location (Young and Maxwell 1992; Trifu et al. 1995; Mansurov 2001; Beck and Brady 2002; Šílený and Milev 2008). It has been shown that these systems greatly facilitate the application of seismic imaging for forecasting geohazards such as rockbursts and collapse at mines (Urbancic and Trifu 2000).

There is a range of factors, including the *b* value, post-event decay, and velocity anomalies, that can be used to examine and estimate the potential for seismic hazards (Hudyma and Potvin 2010; Vallejos and McKinnon 2010; Omi et al. 2013; Westman et al. 2017). Simply locating and visualizing seismic events are less reliable for investigating geological evidence of degradation consistently due to the complexity of shear zones and damage zones (Snelling et al. 2013). Studies have provided examples showing that seismic imaging is a predictive tool for remotely and noninvasively measuring stress conditions within a rock mass (Seebold

Revise and resubmit to Rock Mechanics and Rock Engineering.

✉ Xu Ma
xuma@vt.edu

[1] Department of Mining and Minerals Engineering, Virginia Tech, Blacksburg, VA 24060, USA

[2] Division of Mining and Geotechnical Engineering, Luleå University of Technology, Luleå, Sweden

[3] Creighton Mine, Vale Canada Limited, Sudbury, ON, Canada

[4] Mining and Mineral Processing TEC, Vale Canada Limited, Sudbury, ON, Canada

et al. 1999; Luxbacher et al. 2008; Inbal et al. 2015). Seismic tomographic imaging supports the process of gathering information from discrete seismic events and turning it into a continuous map of stress distribution by building and examining velocity change modeling. Seismic tomography applied at mines images and maps how velocity anomalies transfer and it can be key to subsurface structural characteristics for seismic hazard mitigation of mines. These studies have documented procedures to incorporate seismic events to comprehensively assess geomechanical response and stress evolution (Young and Maxwell 1992; Friedel et al. 1997; Krauß et al. 2014; Ma et al. 2016; Baig et al. 2017; Leake et al. 2017).

The background for this research was that insufficient attention has been given to how stress distribution evolves along with occurrence of HMSE at underground mines. This research aims to investigate temporal and spatial stress evolution around HMSE at a hard-rock underground mine, thus mitigating seismic hazards and improving safety of deep hard-rock underground mines. Methods of seismic event density visualization and passive seismic tomographic imaging were applied in this work to examine stress redistribution and rock mass behavior related to two HMSE. The research computed the evolution of velocity anomalies linked to HMSE and examined stress redistribution by examining velocity anomalies.

2 Data and Methods

2.1 Site Description

This work studied historical seismicity that occurred at Creighton Mine, a deep nickel mine that is located near Sudbury, Ontario with main production areas ranging in depth from 1800 m to 2500 m. Mining methods at the site have evolved over the mine life and the current mining approach is the large-diameter blasthole method. Details of the geological environment and structures of Creighton Mine have been described in previous studies (Beck and Brady 2002; Malek et al. 2008; Snelling et al. 2013). Considerable subsurface seismic occurrences with mining activity have been triggered by dynamic stress change along geological structures at Creighton Mine. A seismic monitoring system has been employed by Creighton Mine and it has substantially enhanced the understanding of seismic hazards and their relationships with mining excavations at deep hard-rock mines.

2.2 Seismic Monitoring System

To monitor and investigate seismic activities, Creighton Mine has been employing a strong ground motion monitoring system and a microseismic monitoring system, both of which are developed by ESG Solutions. Stations of the strong ground motion monitoring system were installed on the surface above the mine to detect high-magnitude seismicity, which are also called mainshocks, major events, or high magnitude seismic events (HMSE). In the strong ground motion monitoring system (Paladin system), three triaxial 4.5 Hz geophones were installed at the surface with a 24-bit data acquisition and recording system. All HMSE in this study were recorded by this strong ground motion monitoring system. The microseismic monitoring system at the time of this study included ten triaxial stations and 52 uniaxial stations to enable sufficient coverage of the rock mass surrounding the main production areas. All these sensors formed a 104-channel mine-wide underground array. Triaxial stations, with sensitivity of 0.3 and 0.5 V/g and a frequency range of 3–8000 Hz, were used to detect source parameters, including magnitude, energy, source radius, and apparent stress. Uniaxial stations with a sensitivity of 30 V/g and a frequency range of 500–5000 Hz were used to record waveform arrival times and locate seismic events through a dense sensor network, which was enabled by their relatively low cost. Figure 1 shows production drifts, microseismicity, HMSE, and the network of microseismic monitoring stations in plan view and longitudinal view. The induced microseismicity was well covered by the seismic network, ensuring accurate event location and waveform capture.

2.3 High Magnitude Seismic Events (HMSE) and Tomography Studies

The data sets studied included roughly 46,500 microseismic events, spatially ranging from 1500 to 2700 m depths, taken from the April to October, 2011 timeframe. Two HMSE were detected within this period: the first HMSE occurred on July 6, 2011 and the second HMSE was triggered 4 days later (July 10, 2011). Precise time of occurrence and location information are listed in Table 1 and spatial distribution of HMSE is shown in Fig. 1. Seismicity was spatially concentrated around the 7530 L, 7680 L, and 7810 L drift (Fig. 1) due to the fact that mining production and backfilled stopes were located nearby. A long-term profile of daily and cumulative event count from April to October, 2011 is illustrated in Fig. 2a. Figure 2b focuses the timeline on the occurrence of HMSE and the associated cumulative and daily seismicity. The time period of each HMSE had a significantly high median daily event rate of seismicity that was observed to be 6–10 times higher than the average median daily event rate. The evolution of the cumulative event count shows an abrupt increase with the occurrence of HMSE. We found that periods containing HMSE appeared to occur in conjunction with high levels of seismicity rate. In addition, another high seismicity rate was found in the middle of August (Fig. 2)

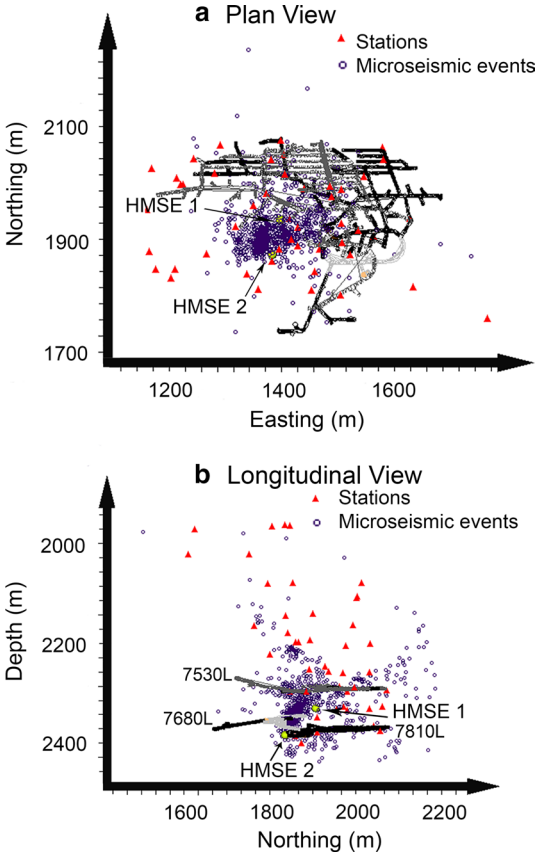

Fig. 1 Three-dimensional plots of the seismic monitoring system and drifts at Creighton Mine: **a** plan view of stations network, microseismic events, and HSME **b** longitudinal view of stations network, microseismic events, and HMSE

without any HMSE occurrence. The increase of seismicity in this period corresponded to ore production blasts. Different patterns of cumulative seismicity were observed around each HMSE. HMSE 1 was triggered in the middle of the significant rate increase, whereas HMSE 2 occurred at the beginning of a significant increase (Fig. 2). Forecasting the occurrence of HMSE purely based on seismicity rate was perceived to be unreliable based on the temporal uncertainty of the abnormal seismicity rate.

Abundant seismicity within relatively short periods from the Creighton Mine data allowed an assessment of change and transfer of velocity anomalies using seismic tomographic tools in a short term. Stress redistribution around HMSE exerts a strong influence on subsequent seismicity. The occurrence of HMSE redistributes stress, and leads to a reduction in stress. By inferring stress distribution from velocity distribution, the temporal and spatial stress changes were estimated at Creighton Mine and particularly around HMSE. To perform tomographic studies, microseismic events that preceded HMSE and their corresponding P-wave arrival times were referenced. Travel times along multiple propagation raypaths from each microseismic event to the sensors that captured this event were then determined. The double-difference tomographic tool TomoDD was employed to perform velocity structure inversions of P-wave propagations. TomoDD, developed by Zhang and Thurber (2003a), uses both relative and absolute arrival times to simultaneously solve seismicity locations and velocity structures (Zhang and Thurber 2003b). The term 'double difference' represents the difference between observed and calculated differential arrival times for two closely located events. The subtraction of travel times using these paired events substantially improve the accuracy of locating events and referring velocity distributions. The arrival time T_k^i is described using the format of a path integral,

$$T_k^i = \tau_i + \int_k^i u \mathrm{d}s, \tag{1}$$

where τ_i is the trigger time of seismic event i, k is the seismic station ID, u is the slowness field, and the element of path length is represented by ds.

The double difference residual $\mathrm{d}r_k^{ij}$ is computed by

$$\mathrm{d}r_k^{ij} = (t_k^i - t_k^j)^{\mathrm{obs}} - (t_k^i - t_k^j)^{\mathrm{cal}}, \tag{2}$$

where $(t_k^i - t_k^j)^{\mathrm{obs}}$ is the difference in the observed arrival times between events i and j, and $(t_k^i - t_k^j)^{\mathrm{cal}}$ is the difference in the calculated travel times between events i and j.

HMSE data with spatial and temporal information and microseismicity, mainly including arrival times of P-wave, seismicity locations, and sensors locations, was acquired from the strong ground motion monitoring system and microseismicity monitoring system. First, we computed travel times, which are propagation times of waveforms from seismic sources to sensors, using related arrival times, event locations, and sensor locations. Then, we computed

Table 1 Times, locations, and moment magnitude of high magnitude seismic events (HMSE) at Creighton Mine

HMSE	Date	Time	North (m)	East (m)	Depth (m)	Moment magnitude
1	July, 6th 2011	8:41 AM	1927	1399	2332	3.1
2	July, 10th 2011	2:44 AM	1861	1384	2391	1.4

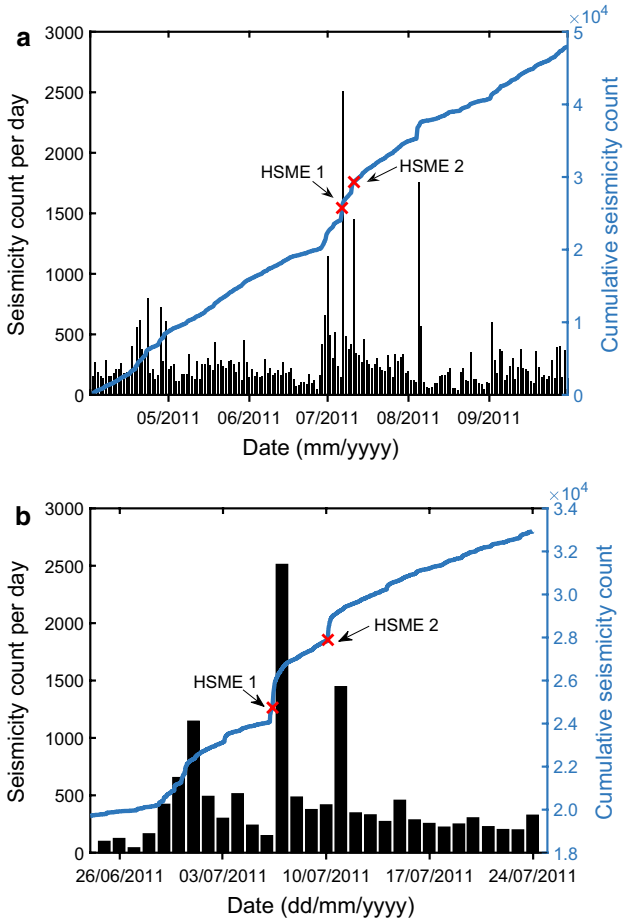

Fig. 2 Cumulative number of microseismic events (solid line) and seismic rate per day (histogram) in **a** a large period of time from April to October in 2011 and **b** a small period containing two HMSE. Red crosses represent HMSE. HMSE 1 occurred on July 6th, 2011 with moment magnitude of 3.1, and HMSE 2 appeared on July 10th, 2011 with moment magnitude of 1.4. Detailed time and locations of the events are shown in Table 1

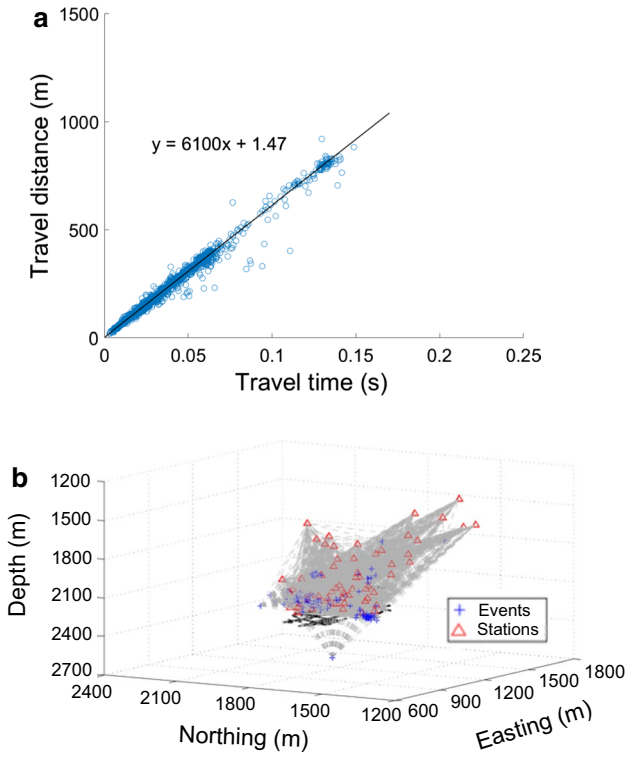

Fig. 3 **a** Linear regression of P-wave travel time versus travel distance. The blue circle represents the travel distance and the corresponding travel time of P-wave propagating from a seismic event to a station. The slope of the black line is used as the average velocity that is assigned to the initial velocity model. **b** The 3D view shows distribution of raypaths from seismic events to seismic stations (color figure online)

the average P-wave velocity by performing linear regression on travel times and corresponding travel distances on all raypaths propagated from events to stations. As is shown in Fig. 3a, the average P-wave velocity was found to be 6100 m/s using linear regression on all raypaths from events to stations in all data sets. For determining the average P-wave velocity, straight raypaths were assumed (Fig. 3b). This P-wave velocity was assigned as the initial, uniform velocity to each grid points of a velocity model, which consists of evenly distributed grid points in a 3-D cubic model (Fig. 4). We constructed this 3-D cubic model using a grid mixed with 24×24×24 m and 48×48×48 m node spacings to establish good coverage for the mining area, including the concentrated seismicity and HSME. A plan view and a top view for grid node distribution with station locations in the microseismic monitoring network are shown in Fig. 4. The tomographic inversion was performed to minimize the residual of arrival times and differential times. The model variance and the data variance are determined by the damping value. Large model perturbations usually result from small damping values, and large damping values cause small model perturbations. It was proposed that the optimal damping value can be selected by a series of single-step inversions (Eberhart-Phillips 1986). We performed a trade-off analysis with plotting data variance versus model variance of the P-wave velocity model to look for the preferred damping value. Using trade-off analysis to locate the elbow point in the trade-off curve, the optimal damping value was determined as 400 for best balancing the roughness and the stabilization of the model (Fig. 5). By implementing appropriate iterations using the preferred damping value obtained from trade-off analysis, updated velocity values were generated from the velocity inversion process to replace the initial, uniform velocity model during each iteration until the optimal velocity structure was achieved.

Microseismicity was separated temporally surrounding each HMSE into two groups: the first group, termed the 'pre-HMSE group,' only included events before HMSE and the second group, the 'pre-and-post-HMSE group,'

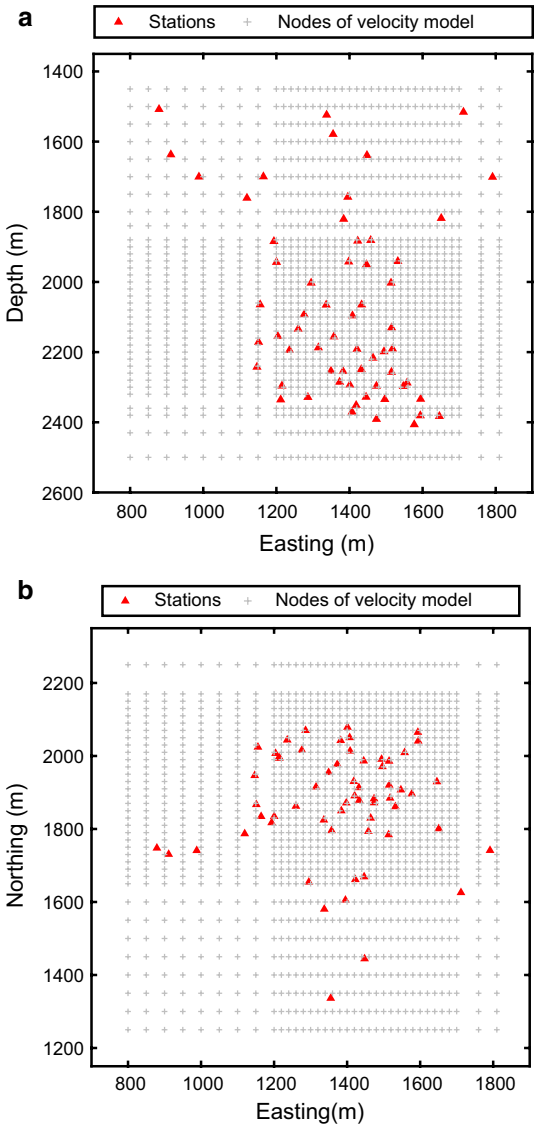

Fig. 4 **a** The lateral view and **b** the top view of nodes distribution in the cubic velocity model

included all other events on the day of HMSE combined with events from the first group. Thus four groups of events were allocated for two HMSE. Tomographic inversion was then conducted using these data sets to generate seismic images and determine velocity anomalies for each data set. To verify the reliability of the velocity model, standard deviations of each tomogram were computed. It was found that they significantly reduced with additional inversion iterations and 25 iterations were conducted for each group in these tomographic studies (Fig. 6 and Fig. 7). Table 2 shows the periods that were used in this study. Velocity anomalies were compared to summarize variations between them and are interpreted in the results section. To explicitly ascertain stress evolution around

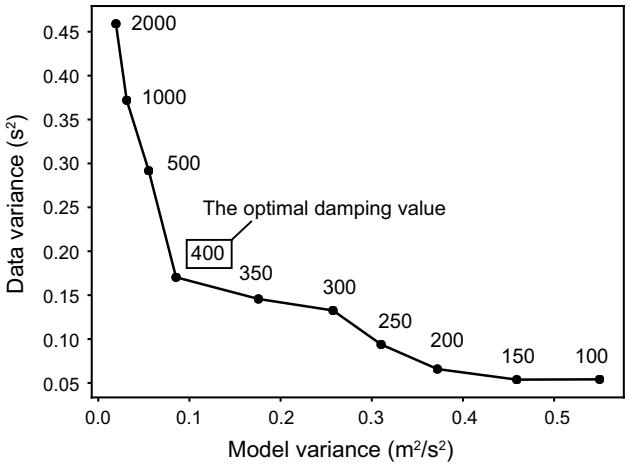

Fig. 5 Trade-off curve analysis for choosing optimal damping for velocity inversion. The damping value 400 at the elbow point of the curve is selected as the optimal damping value

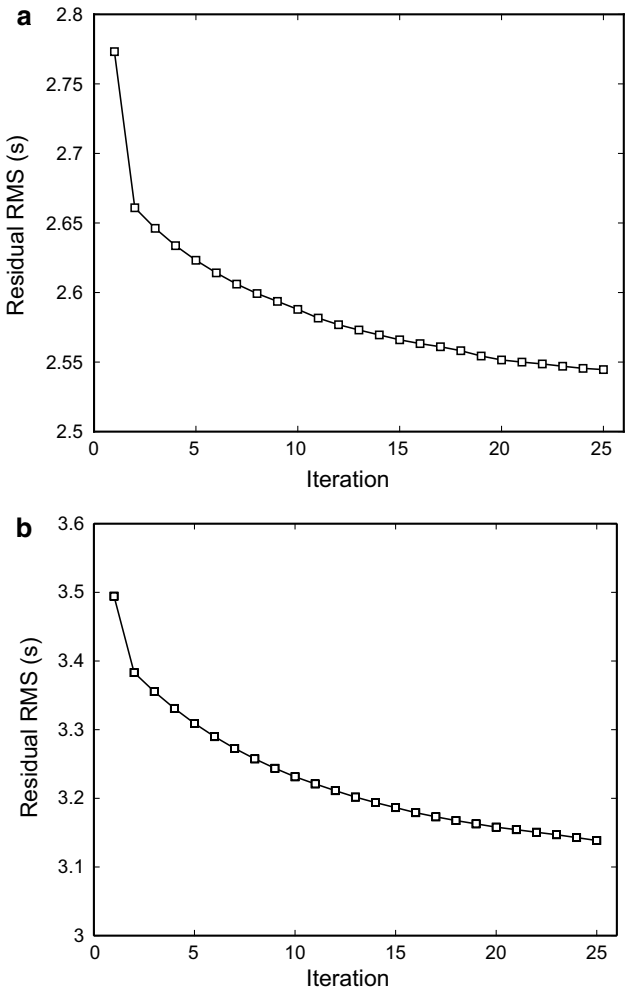

Fig. 6 Residual RMS for **a** pre-HMSE group and **b** pre-and-post-HMSE group of HMSE 1

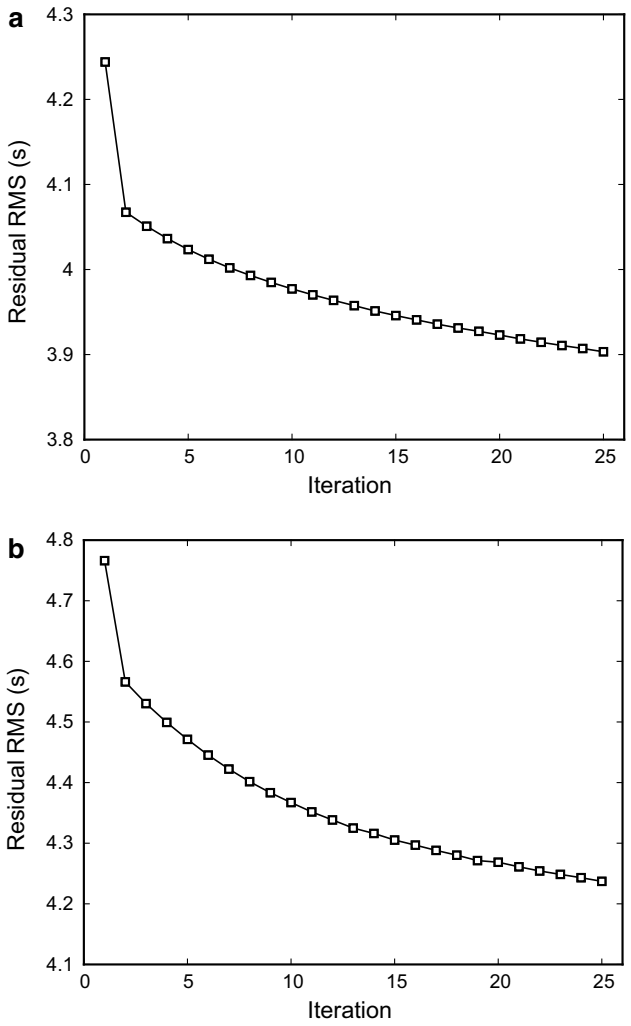

Fig. 7 Residual RMS for **a** pre-HMSE group and **b** pre-and-post-HMSE group of HMSE 2

HMSE, a differential tomogram was obtained by subtracting velocity distributions from the pre-HMSE group to the pre-and-post-HMSE group.

3 Results

3.1 Seismicity Density Map

Two methods, examining spatial density of seismicity and tomographic imaging velocity distribution, were employed to help understand stress redistribution and rock mass behavior with two 2011 HMSE at Creighton Mine. To show spatial distribution of seismicity at Creighton Mine, a seismicity map was plotted across continuous, incremental depth ranges to show the spatial distribution of seismicity density. Figure 8e displays the distribution of the density of seismic events including all 46,500 events across all depths. Only a few events were located above 1800 m due to the fact that minimal mining activity was performed above this depth, while some zones below 1800 m were very seismically active. Seismicity progressively concentrated and the area of the seismically active region kept expanding with increasing depth. Most of the recorded seismicity was located below 2000 m and the seismicity density experienced a dramatic growth beneath 2200 m (Fig. 8e). Both horizontal (Fig. 8a–c) and vertical (Fig. 8d) views indicate that HMSE occurred in zones hosting the highest density of seismicity. Figure 8a shows scarce events with a very low density for depths from 1300 to 1800 m. Conversely, depths from 1800 to 2300 m showed a higher density distribution, but only included a small portion of events in the whole volume (Fig. 8b). A high-density zone that appeared to the east of 1400 m and north of 1900 m was correlated with production and development blasting activity. The other high-density zone was found in easting 1300 m and northing 1800 m where a lower tip of a shear zone was located (Fig. 8b). The section of depths between 2300 m and 2800 m was targeted as an emphasized region that experienced the most intensive seismic density among all levels (Fig. 8c). The drifts were surrounded by four high seismic density regions. The region with the highest seismic density was located at the same region identified in the 1800–2300 m depth interval, but with a larger area due to abundant seismicity. As shown in the plan view of depth between 2300 m and 2800 m, HMSE 1 and HMSE 2 were located near the borders of the high seismic density region. A series of adjacent stopes in close proximity to the two HMSE were developed several months

Table 2 Time frames of tomography studies

Time frames	Start	End	Number of travel time picks used
1	July 1st, 2011 0:00 AM	July 6th, 2011 8:00 AM	22,347
2	July 1st, 2011 0:00 AM	July 7th, 2011 0:00 AM	58,120
3	July 8th, 2011 0:00 AM	July 10th, 2011 0:00 AM	9345
4	July 8th, 2011 0:00 AM	July 11th, 2011 0:00 AM	26,607

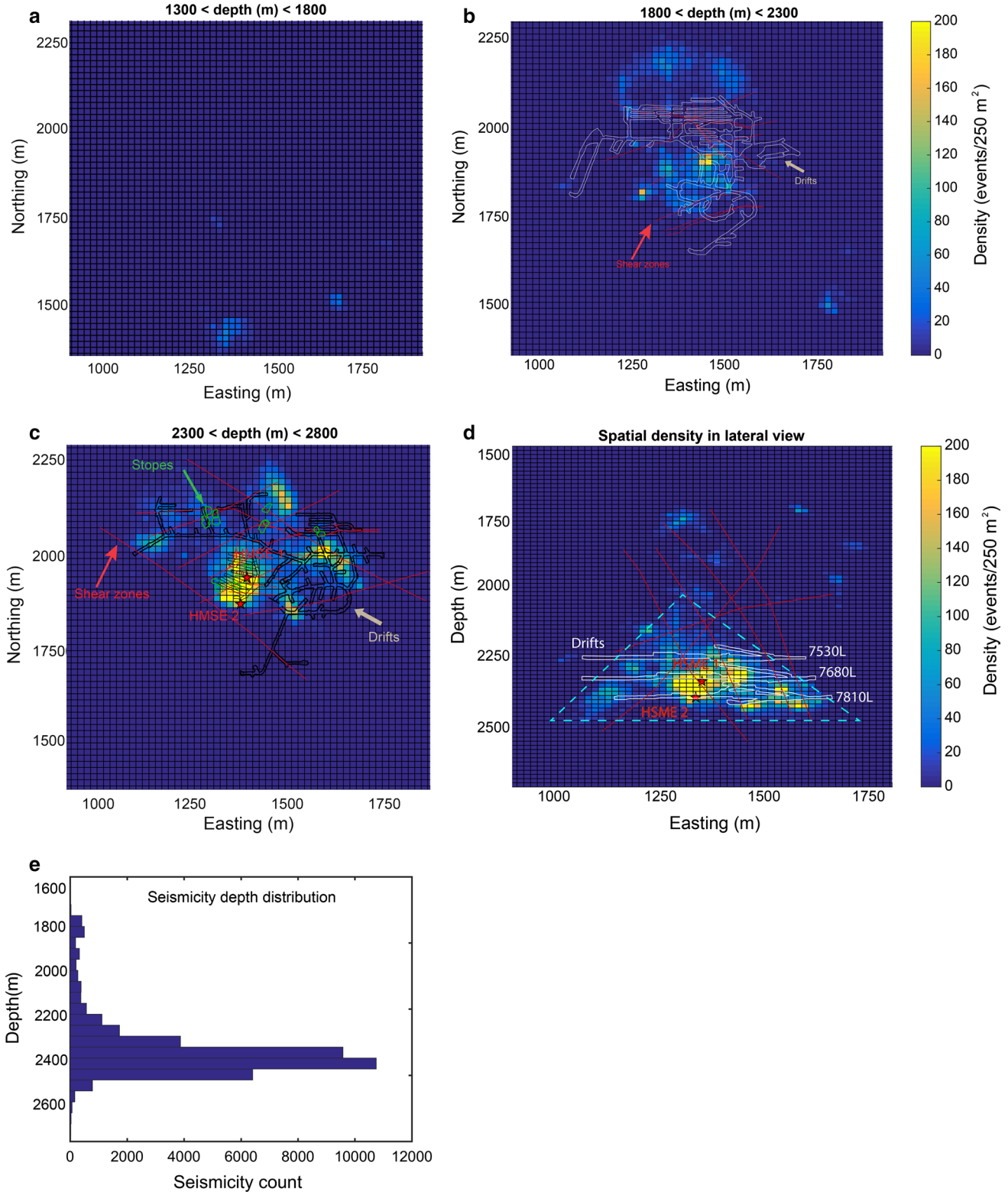

Fig. 8 Spatial distribution of seismicity density from April to October, 2011 at Creighton Mine. Plan views of seismicity density are indicated in the following depth ranges: **a** 1300–1800 m, **b** 1800–2300 m, and **c** 2300–2800 m. Areas with intense seismicity are noted in yellow; areas devoid of seismicity are shown in blue. **d** The density map of longitudinal view (vertical cross section). **e** Microseismicity depth distribution (color figure online)

prior to their occurrence. This major high-density region was also crossed by dense shear zones, including two major shear zones trending at 45° and three small-size horizontal shear zones. Factors such as stope excavation and shear zones were likely to mutually cause the occurrence of HMSE. In addition, three other regions with a substantially high density of seismicity, but with smaller areas, were found.

In the longitudinal section view (Fig. 8d), the area with the largest seismic density was observed to range from 2300 m to 2400 m in depth. In a similar fashion to the plan view, HMSE appeared within the region associated with the largest seismicity density: HMSE 1 was located at 7680L drift and HMSE 2 was located at 7810L drift. Underground development with more branches further east showed additional small areas with higher densities. Interestingly, the whole distribution of this density map is shaped like a triangle (delineated in Fig. 8d), where increasing volumes of microseismic events are distributed more extensively with greater depths. A likely explanation for this phenomenon is that the overburden stress increases with the greater depth, thus triggering more events in the fracture development process.

3.2 Velocity Distributions with HMSE

A series of tomograms for each period was calculated and a horizontal slice at 2360 m depth, which is slightly above the 7680 drift, at the identical location was picked to compare across the time periods. By analyzing the tomograms, stress variation was inferred to review stress redistribution influenced by HMSE. Evident velocity anomalies emerged near the target region. Areas in warm colors illustrate high-velocity regions and low-velocity regions are exhibited in cold colors.

During the periods of our study, the primary production levels in the Creighton Mine were in the 7530 level, 7680 level, and 7810 level. These levels were named according to their depths in the units of feet. From the tomogram of pre-HMSE-1 at the 7680 level, there was a striking boundary on N135°E line along the drift, which distinctively divides the tomograms into high- and low-velocity zones (Fig. 9a). The counterpart of pre-and-post-HMSE-1 shows a similar general distribution with results of pre-HMSE-1. Comparing the velocity distribution of pre-HMSE-1 to pre-and-post-HMSE-1, the high-velocity part reduced while the low-velocity area increased to some extent. HMSE 1 was located on the high-velocity area of both pre-HMSE-1 and pre-and-post-HMSE-1 tomograms. It was observed that both the high-velocity region and the low-velocity region tended to shrink in size and intensity when comparing Fig. 9a, b. To investigate the associated change of velocity distributions, velocity anomalies were subtracted between the two time periods (July 1 to July 6 and July 1 to July 7) to generate the velocity differential tomogram shown in Fig. 9c. The velocity distribution of the differential tomogram reveals that the previous low velocity increased a certain amount and the previous high velocity correspondingly decreased with the occurrence of HMSE 1 (Fig. 9c). According to the iso-velocity contour of the differential tomogram (Fig. 9d), it is clearly shown that the previous high-velocity zone that hosted HMSE 1 reduced in spatial extent. In Fig. 9c, high-velocity areas appear to increase from July 6 to July 7, while velocity in low-velocity areas continues to decrease from July 6 to July 7. The seismic differential tomogram indicates that the proximity of HMSE 1 decreased by about 350 m/s and this was inferred to a corresponding stress relaxation caused by HMSE 1.

The epicenter of HMSE 2 was 70 m further to the southwest (on plan) of HMSE 1's epicenter and HMSE 2 occurred 60 m above (in longitudinal view) HMSE 1. Two major high-velocity regions, separated by a low-velocity area in the center, emerged in the northeast and southwest around geological structures (Fig. 10a, b). Figure 10a shows that a high-velocity region remained around HMSE in the period of July 8–July 9. Similarly, for the period of July 8–July 10, these velocity anomalies continued to dominate in the same geographic regions, but tended to return to equilibrium (Fig. 10b). Velocity changes were subtracted from July 8–July 10 to July 8–July 9 to examine the differential tomogram and investigate stress redistribution in detail between these two periods. Figure 10c shows that the previous low-velocity region experienced a velocity increase and as expected, the average velocity in the previous high-velocity region decreased. In Fig. 10c, high-velocity areas continue to increase and low-velocity areas exhibit velocity decrease from July 9 to July 10. Velocity differentials changed toward the opposite direction after the HMSE, although high-velocity regions and low-velocity regions still maintained a sharp contrast. Although both tomograms (July 8–July 9 and July 8–July 10) did not indicate any obvious high velocity in the exact location of HMSE 2, HMSE 2 was found to be located at the border of an area with a significant velocity decrease in the differential tomogram (Fig. 10c) and the iso-velocity contour (Fig. 10d). The significant velocity decrease reflected an associated significant stress relaxation in the area in which HMSE 2 was located at its border.

HMSE 1 was located within a shear zone, whereas HMSE 2 appeared to be more in the general vicinity of shear zones and drifts. A realistic interpretation might be that because the rock mass near the drifts or other prior structures had been weakened as a result of released accumulated energy near HMSE 1, HMSE 2 was then triggered in the region that was away from previously formed damage zones.

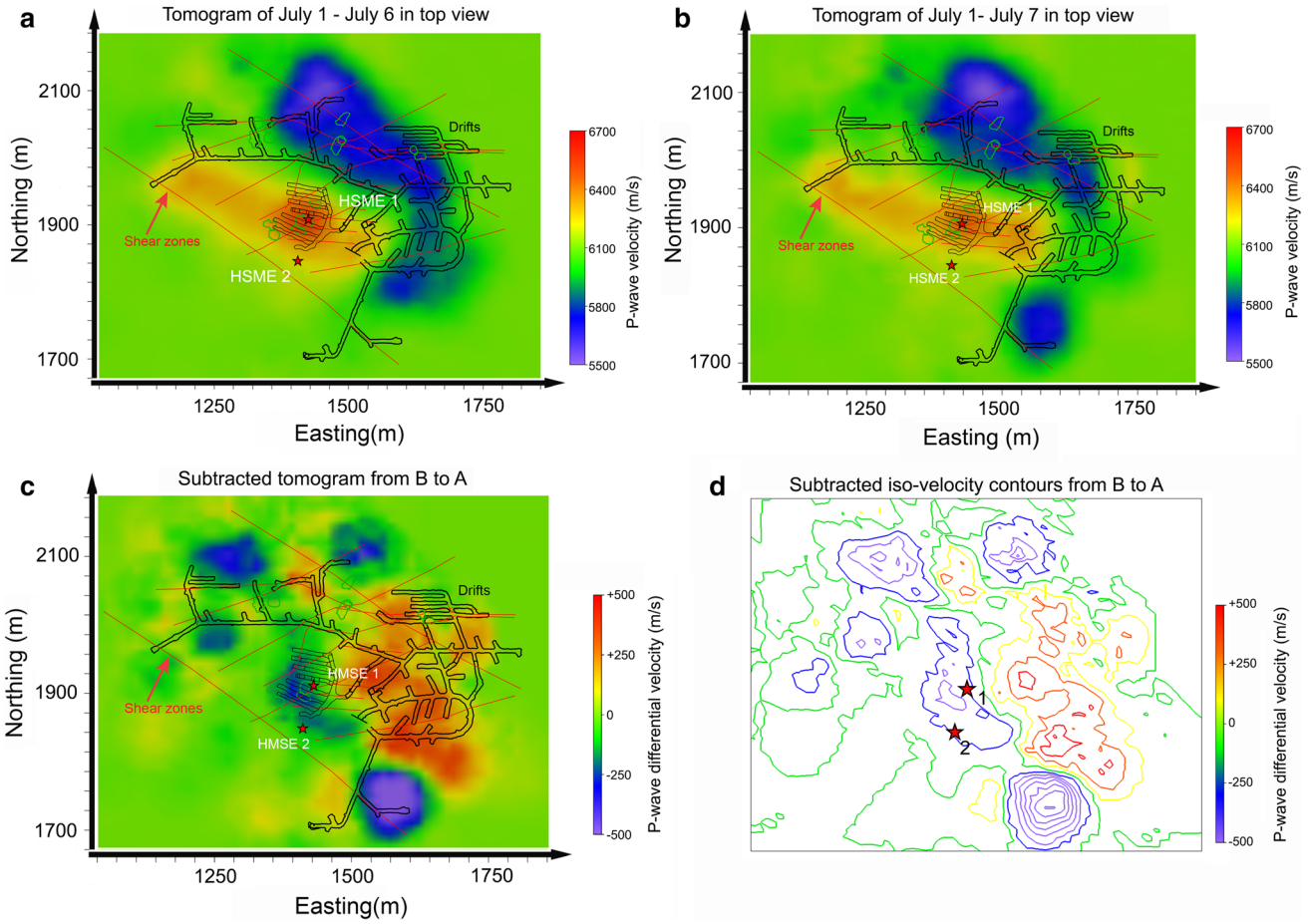

Fig. 9 Plan views of P-wave velocity distribution with occurrence of HMSE 1. **a** Plan view of P-wave velocity distribution in the nearby level of HMSE 1 for period of July 1–July 6. **b** Plan view of P-wave velocity distribution in the nearby level of HMSE 1 for period of July 1–July 7. **c** Differential tomogram in plan view by subtracting P-wave velocity distribution of July 1-July 6 from July 1-July 7. Red areas show velocity increase from July 6 to July 7; blue areas show P-wave velocity decrease from July 6 to July 7. **d** Iso-velocity contours of the differential tomogram (color figure online)

4 Discussion and Conclusions

Measurement of spatial density of seismicity and tomographic imaging of stress distribution to examine the stress redistribution and rock mass behavior related to two events with local magnitude greater than 1.0 in a deep nickel mine have been reported in this paper. Velocity distribution in the subsurface at a hard-rock mine was found to change significantly with the occurrence of HMSE. Relatively high velocity emerged surrounding the geological structures prior to HMSE, especially for HMSE 1. Following the occurrence of HMSE, velocity anomalies in these regions started to change toward equilibrium. That is, high-velocity anomalies decreased and low-velocity anomalies increased based on their previous sharp contrast. HMSE occurred in the boundary of high-velocity regions and were distant from low-velocity areas. A greater high-velocity region and a large spatial density of microseismicity could potentially suggest the occurrence of a future HMSE. The explanation for this change is that stress concentration triggers HMSE, the occurrence of which subsequently causes stress relaxation in the surrounding rock mass.

After the occurrence of HMSE, the nearby high-stress regions evolve toward a more balanced state. This implies that rupture processes with HMSE lead to stress reduction with local geomechanical relaxation. The growth of low-stress regions in turn suggests stress increases to some extent after HMSE, contributing to a newly redistributed stress field. A prior study examined stress change in a mine affected by an HMSE rupture and made similar conclusions using in situ stress measurement combined with focal mechanism data inversion (i.e., stress buildup before HMSE and then reduction in the short term after the event) (Sakaguchi and Yokoyama 2017; Sakaguchi et al. 2017). HMSE's give rise to subsequent stress relaxations and stress concentration in zones distant from the destressing regions, associated

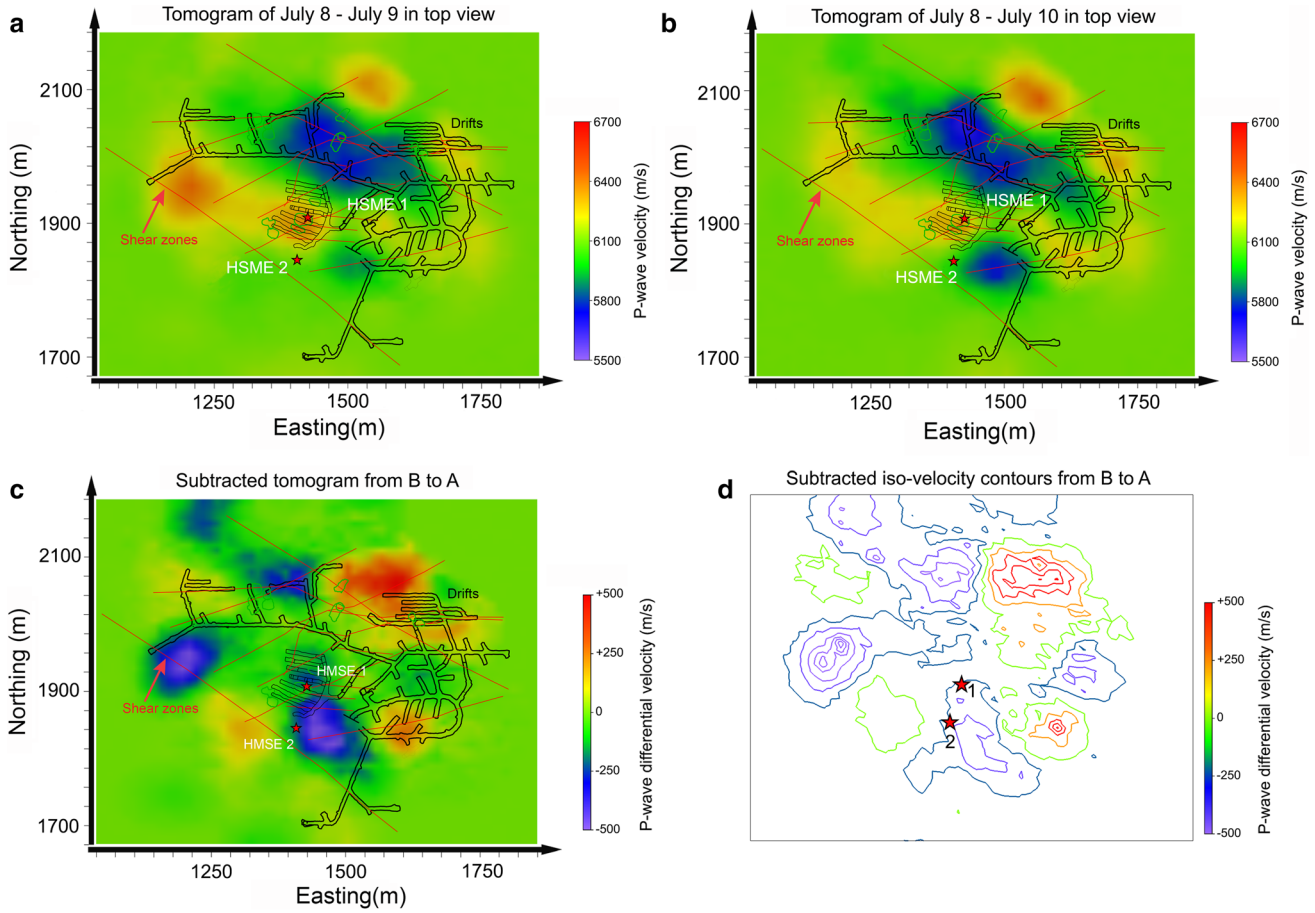

Fig. 10 Plan views of P-wave velocity distribution with occurrence of HMSE 2. **a** Plan view of P-wave velocity distribution in the nearby level of HMSE 2 for period of July 8–July 9. **b** Plan view of P-wave velocity distribution in the nearby level of HMSE 2 for period of July 8–July 10. **c** Differential tomogram in plan view by subtracting P-wave velocity distribution of July 8-July 9 from July 8-July 10. Red areas show P-wave velocity increase from July 9 to July 10; blue areas show P-wave velocity decrease from July 9 to July 10. **d** Iso-velocity contours of the differential tomogram (color figure online)

with velocity increase and velocity reduction in tomographic images.

The occurrence of microseismicity showed weak spatial correlation with the location of shear zones. Some regions with large spatial densities of seismicity in this study overlapped with areas of shear zones, although there were quite a few shear zones in areas where little seismicity was observed. There is, therefore, no obvious correlation between seismicity and mapped shear zones, which is consistent with Snelling's study (Snelling et al. 2013). It is possible that while the effects of shear zones are related to the occurrence of HMSE, most seismicity is triggered by excavation advance and blasting rather than being caused directly by static shear zones. It is possible that stress perturbations from mining-induced seismicity stimulate and activate new, or unobserved, fault systems. A study stated that hurdles remain in identifying and characterizing faults and shear zones in the subsurface; faults of moderate size (100–200 m) ought to be underlined because they are large enough to result in seismicity, on the other hand, traditional techniques often fail to identify them because they are not large enough (White and Foxall 2016). Using passive seismic tomography associated with other geophysical techniques can help to detect and characterize potential faults and shear zones.

Compared to in situ stress measurement, the seismic imaging used in our study is capable of efficiently visualizing 3-D stress evolution and providing temporal-spatial stress evolution in detail. Principal stress orientation data were limited for the purposes of this study. Seismic imaging associated with focal mechanism inversion would ascertain static stress and dynamic stress variations due to HMSE.

Seismic tomographic imaging can make a difference when it comes to the utilization of seismic monitoring systems at mines. HMSE that occur near drifts are high-risk events for mining operations, but there is potential to incorporate seismic tomography as a tool enhance understanding.

Acknowledgements Vale Canada Limited provided the field data for this study. Support for this project came from the Canadian Mining Industry Research Organization and a NIOSH Ground Control Capacity Building grant (contract 200-2011-40313).

References

Baig AM, Bosman K, Urbancic TI (2017) Temporal changes in stress state imaged through seismic tomography. In: proceedings of the eighth international conference on deep and high stress mining. Australian Centre for Geomechanics, pp. 269–274

Beck DA, Brady BHG (2002) Evaluation and application and controlling parameters for seismic events in hard-rock mines. Int J Rock Mech Min Sci 39:633–642

Brady BHG, Brown ET (2013) Rock mechanics: for underground mining. Springer, Netherlands

Eberhart-Phillips D (1986) Three-dimensional velocity structure in northern California Coast Ranges from inversion of local earthquake arrival times. Bull Seismol Soc Am 76(4):1025–1052

Friedel MJ, Scott DF, Williams TJ (1997) Temporal imaging of mine-induced stress change using seismic tomography. Eng Geol 46:131–141

Hudyma M, Potvin YH (2010) An engineering approach to seismic risk management in hardrock mines. Rock Mech Rock Eng 43(6):891–906

Inbal A, Clayton RW, Ampuero JP (2015) Imaging widespread seismicity at midlower crustal depths beneath Long Beach, CA, with a dense seismic array: evidence for a depth-dependent earthquake size distribution. Geophys Res Lett 42:6314–6323

Krauß F, Giese R, Alexandrakis C, Buske S (2014) Seismic travel-time and attenuation tomography to characterize the excavation damaged zone and the surrounding rock mass of a newly excavated ramp and chamber. Int J Rock Mech Min Sci 70:524–532

Leake MR, Conrad WJ, Westman EC et al (2017) Microseismic monitoring and analysis of induced seismicity source mechanisms in a retreating room and pillar coal mine in the Eastern United States. Undergr Sp 2:115–124

Luxbacher K, Westman E, Swanson P, Karfakis M (2008) Three-dimensional time-lapse velocity tomography of an underground longwall panel. Int J Rock Mech Min Sci 45:478–485

Ma X, Westman EC, Fahrman BP, Thibodeau D (2016) Imaging of temporal stress redistribution due to triggered seismicity at a deep nickel mine. Geomechanics for Energy and the Environment 5:55–64

Malek F, Espley S, Yao M, Trifu C (2008) Management of high stress and seismicity at Vale Inco Creighton Mine. In: the 42nd US rock mechanics symposium (USRMS). American rock mechanics association

Malek F, Suorineni FT, Vasak P (2009) Geomechanics strategies for rockburst management at vale inco creighton mine. In: ROCKENG09: proceedings of the 3rd Canada-US rock mechanics symposium, vol 4234. p 12

Mansurov VA (2001) Prediction of rockbursts by analysis of induced seismicity data. Int J Rock Mech Min Sci 38:893–901

Omi T, Ogata Y, Hirata Y, Aihara K (2013) Forecasting large aftershocks within one day after the main shock. Sci Rep 3:2218

Sakaguchi K, Yokoyama T (2017) Changes in in situ rock stress before and after the major 2011 Tohoku-Oki earthquake. Procedia Eng 191:768–775

Sakaguchi K, Yokoyama T, Lin W, Watanabe N (2017) Stress buildup and drop in inland shallow crust caused by the 2011 Tohoku-oki earthquake events. Sci Rep 7:10242

Seebold I, Lehmann B, Arribas A et al (1999) Development of tomographic systems for mining, mineral exploration and environmental purposes. Trans Inst Min Metall Sect B Applied Earth Sci 108:105–118

Šílený J, Milev A (2008) Source mechanism of mining induced seismic events—resolution of double couple and non double couple models. Tectonophysics 456:3–15

Snelling PE, Godin L, McKinnon SD (2013) The role of geologic structure and stress in triggering remote seismicity in Creighton Mine, Sudbury, Canada. Int J Rock Mech Min Sci 58:166–179

Sweby G, Trifu C, Goodchild D, Morris L (2006) High resolution seismic monitoring at Mt Keith open pit mine. In: Golden rocks 2006, The 41st US symposium on rock mechanics (USRMS). American Rock Mechanics Association

Trifu CI, Urbancic TI, Young RP (1995) Source parameters of mining-induced seismic events: an evaluation of homogeneous and inhomogeneous faulting models for assessing damage potential. Pure Appl Geophys 145:3–27

Urbancic T, Trifu C (2000) Recent advances in seismic monitoring technology at Canadian mines. J Appl Geophys 45(4):225–237

Vallejos J, McKinnon S (2010) Omori's law applied to mining-induced seismicity and re-entry protocol development. Pure Appl Geophys 167(1–2):91–106

Vallejos J, McKinnon S (2011) Correlations between mining and seismicity for re-entry protocol development. Int J Rock Mech Min Sci 48:616–625

Westman EC, Luxbacher K, Schafrik S (2012) Passive seismic tomography for three-dimensional time-lapse imaging of mining-induced rock mass changes. Lead Edge 31(3):338–345

Westman EC, Molka RJ, Conrad WJ (2017) Ground control monitoring of retreat room–and–pillar mine in Central Appalachia. Int J Min Sci Technol 27:65–69

White JA, Foxall W (2016) Assessing induced seismicity risk at CO_2 storage projects: recent progress and remaining challenges. Int J Greenh Gas Control 49:413–424

Young RP, Maxwell SC (1992) Seismic characterization of a highly stressed rock mass using tomographic imaging and induced seismicity. J Geophys Res Earth 97:12361–12373

Young R, Collins D, Reyes-Montes J (2004) Quantification and interpretation of seismicity. Int J Rock Mech Min Sci 41:1317–1327

Zhang H, Thurber C (2003a) User's manual for tomoDD1. 1 (double-difference tomography) for determining event locations and velocity structure from local earthquakes and explosions. Department of geology and geophysics. University of Wisconsin–Madison, Madison

Zhang H, Thurber CH (2003b) Double-difference tomography: the method and its application to the Hayward fault, California. Bull Seismol Soc Am 93(5):1875–1889